Editors' Suggestion

Hydrodynamic Relaxation in a Strongly Interacting Fermi Gas

Xin Wang, Xiang Li, Ilya Arakelyan, and J. E. Thomas*
Department of Physics, North Carolina State University, Raleigh, North Carolina 27695, USA

(Received 1 December 2021; revised 13 January 2022; accepted 8 February 2022; published 3 March 2022)

We measure the free decay of a spatially periodic density profile in a normal fluid strongly interacting Fermi gas, which is confined in a box potential. This spatial profile is initially created in thermal equilibrium by a perturbing potential. After the perturbation is abruptly extinguished, the dominant spatial Fourier component exhibits an exponentially decaying (thermally diffusive) mode and a decaying oscillatory (first sound) mode, enabling independent measurement of the thermal conductivity and the shear viscosity directly from the time-dependent evolution.

DOI: 10.1103/PhysRevLett.128.090402

Studies of thermodynamics and hydrodynamic transport in strongly correlated Fermi gases connect widely different forms of matter across vast energy scales [1–3]. Strongly interacting Fermi gases are created by tuning a trapped, two-component cloud near a collisional (Feshbach) resonance [4]. A resonantly interacting or unitary Fermi gas is of special interest, as it is a scale-invariant, strongly interacting quantum many-body system, with thermodynamic and transport properties that are universal functions of the density and temperature [5], permitting parameter-free comparisons with predictions.

However, the behavior of the shear viscosity η and the thermal conductivity κ_T of a unitary Fermi gas is not yet established. Measurement of hydrodynamic flow in freely expanding clouds [6,7] enables extraction of η in the normal fluid regime, but requires a second order hydrodynamics model to properly account for ballistic flow in the dilute edges [8,9]. Recent measurements of the sound diffusivity [10], by sound attenuation in a driven, uniform density, unitary Fermi gas, constrain η and κ_T, but they are not independently determined [11].

In this Letter, we report new time-domain, free evolution methods for measuring hydrodynamic transport coefficients in a normal fluid unitary Fermi gas. We confine a cloud of ^{6}Li atoms in a repulsive box potential, producing a sample of nearly uniform density. A density perturbation is then created, Fig. 1, by applying a small static optical potential that is spatially periodic along one axis. After equilibrium is established, the perturbing potential is abruptly extinguished. We measure the time dependence of the dominant spatial Fourier component of the density, $\delta n(q,t)$, Fig. 2, which exhibits an exponentially decaying mode that measures the thermal conductivity and a decaying oscillatory mode that determines the sound speed and the sound diffusivity. The data are well fit by a linear hydrodynamics analytic model, enabling measurement of both the shear viscosity η and the thermal conductivity κ_T.

The experiments employ ultracold ^{6}Li atoms in a balanced mixture of the two lowest hyperfine states, which are evaporatively cooled in a CO_2 laser trap and loaded into a box potential. The box comprises six sheets of blue-detuned light, created by two digital micromirror devices (DMDs) [12]. The top and bottom sheets employ a 669 nm beam. The four vertically propagating sheets are produced by a 532 nm beam, which passes through a diffractive optical element and an imaging lens to produce a "top-hat" shaped intensity profile on the surface of the DMD array. The box potential $U_0(\mathbf{r})$ yields a rectangular density profile with typical dimensions $(x,y,z) = (52 \times 50 \times 150)$ μm. The density varies slowly in the direction of the long (z) axis, due to the harmonic confining potential $\propto z^2$ arising from the curvature of the bias magnetic field, which has little effect on the shorter x and y axes. The typical total central density is $n_0 = 4.5 \times 10^{11}$ atoms/cm^3, with the Fermi energy $\epsilon_{F0} \equiv k_B T_F = k_B \times 0.22$ μK and Fermi speed $v_F \simeq 2.5$ cm/s. The box depth $U_0 \simeq 1.1$ μK [13].

Once the cloud is loaded into the box potential, we employ the 532 nm DMD to slowly ramp up an additional small optical potential $\delta U(z)$, which is spatially periodic along the z axis. After thermal equilibrium is established, the cloud profile exhibits a periodic spatial modulation, $\delta n(z,0)$, Fig. 1. The measurements employ modulation amplitudes $\delta n/n_0$ from 7% to 19%, yielding consistent data within our error bars.

After the periodic potential is abruptly extinguished, we measure the oscillatory decay of the density change $\delta n(z,t) = n(z,t) - n_0(z)$. For each image, the signal n and subtracted background $n_0(z)$ densities are scaled to their respective total atom number to suppress noise arising from shot to shot atom number variation. We perform a fast Fourier transform (FFT) of $\delta n(z,t)$ at each time, in a region containing an integer number (typically 3–4) of spatial periods near the peak density, minimizing the imaginary component to obtain a real transform, $\delta n(q,t)$, Fig. 2.

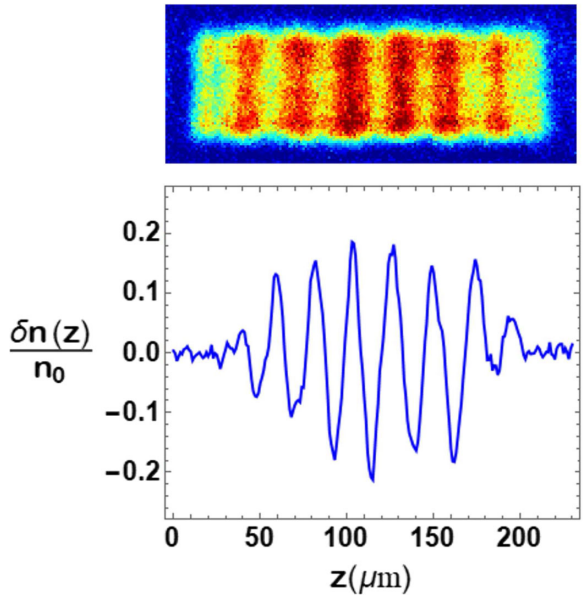

FIG. 1. A unitary Fermi gas is loaded into a box potential with a small static spatially periodic perturbation δU, creating a spatially periodic 1D density profile. After δU is abruptly extinguished, the dominant Fourier component exhibits a two-mode oscillatory decay (see Fig. 2).

To model the data, where the initial conditions are isothermal, it is convenient to construct the coupled equations for the changes in the density $\delta n(z,t)$ and temperature $\delta T(z,t)$. We use the continuity equation to eliminate the velocity field. For experiments in the linear response regime [13],

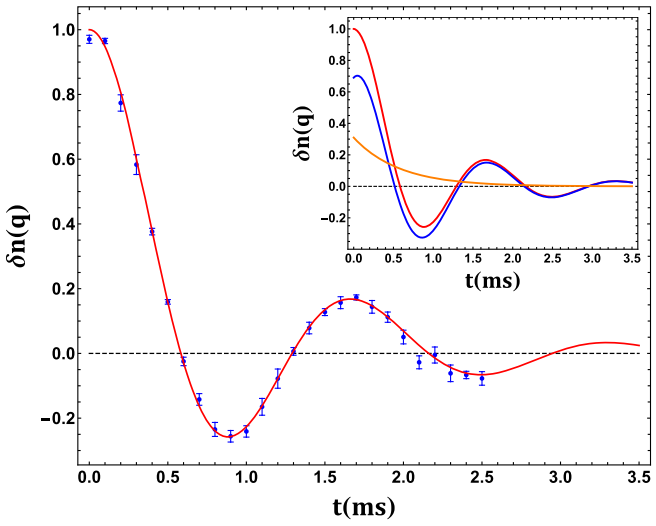

FIG. 2. Real part of the Fourier transform of the density perturbation $\delta n(q,t)$ for $q = 2\pi/\lambda$ with $\lambda = 22.7$ μm. The reduced temperature $T/T_F = 0.46$. Blue dots (data); Red curve: analytic hydrodynamics model, Eq. (3). Inset shows contributions of thermal diffusion (orange exponential) and first sound (blue). The error bars are the standard deviation of the mean of $\delta n(q,t)$ for 5–8 runs, taken in random time order.

$$\delta\ddot{n} = c_T^2\partial_z^2(\delta n + \delta\tilde{T}) + \frac{\frac{4}{3}\eta + \xi_B}{n_0 m}\partial_z^2\delta\dot{n} + \frac{1}{m}\partial_z[n_0(z)\partial_z\delta U + \delta n\partial_z U_0(z)], \quad (1)$$

with c_T the isothermal sound speed and m the atom mass. Here, $\delta\tilde{T} = n_0\beta\delta T$ has dimension of density, with $\beta = -1/n(\partial n/\partial T)_P$ the thermal expansivity [13] and

$$\delta\dot{\tilde{T}} = \epsilon_{\rm LP}\,\delta\dot{n} + \frac{\kappa_T}{n_0\,c_{V_1}}\partial_z^2\delta\tilde{T}, \quad (2)$$

with $\epsilon_{\rm LP} \equiv c_{P_1}/c_{V_1} - 1$ the Landau-Placzek parameter. The heat capacities per particle at constant volume c_{V_1} and at constant pressure c_{P_1} can be determined from the measured equation of state [13,14].

Equations (1) and (2) have simple physical interpretations. The c_T^2 terms on the right-hand side of Eq. (1) correspond to the pressure change [13]. A viscous damping force arises from the shear viscosity, $\eta \equiv \alpha_\eta\hbar n_0$, while the bulk viscosity ξ_B vanishes for a unitary Fermi gas [15]. The final terms in Eq. (1) arise from the perturbing and box potentials, where $\partial_z U_0(z)$ is found from the slowly varying background density $n_0(z)$ [13] and $\delta U(z, t > 0) = 0$ for our experiments. The first term on the right-hand side of Eq. (2) describes the adiabatic change in the temperature due to the change in density. The last term describes temperature relaxation at constant density due to the heat flux, which is proportional to the thermal conductivity $\kappa_T \equiv \alpha_\kappa\hbar n_0 k_B/m$. Equations (1) and (2) can be solved numerically for $\delta n(z,t)$, with the initial conditions $\delta n(z,0)$ (measured), $\delta\dot{n}(z,0) = 0$, and $\delta\tilde{T}(z,0) = 0$.

We find that a perturbation wavelength $\lambda \simeq 23$ μm yields good dynamic range for decay measurements over time scales that avoid perturbing $\delta n(z,t)$ in the measured central region by reflections from the walls of box potential, which then can be neglected. Since $\delta U = 0$, a spatial Fourier transform of Eqs. (1) and (2) yields coupled equations for $\delta\ddot{n}(q,t)$ and $\delta\dot{\tilde{T}}(q,t)$. These determine the analytic fit function [13],

$$\delta n(q,t) = A_0 e^{-\Gamma t} + e^{-at}[A_1\cos(bt) + A_2\sin(bt)], \quad (3)$$

where $A_1 = A - A_0$ and $A_2 = [(\Gamma - a)A_0 + aA]/b$ satisfy two of the initial conditions $\delta n(q,0) = A$ and $\delta\dot{n}(q,0) = 0$. The third initial condition $\delta\ddot{n}(q,0) = -c_T^2 q^2 A$ [13] determines $A_0 = A(a^2 + b^2 - c_T^2 q^2)/[(\Gamma - a)^2 + b^2]$.

We see that the solution consists of two independent modes, Fig. 2 (inset). One mode is exponentially decaying and determines the thermal diffusivity as discussed below. The other is a decaying, oscillating first sound mode, which determines the sound diffusivity. Together, the decay rates of these two distinct modes determine both the thermal conductivity and the shear viscosity.

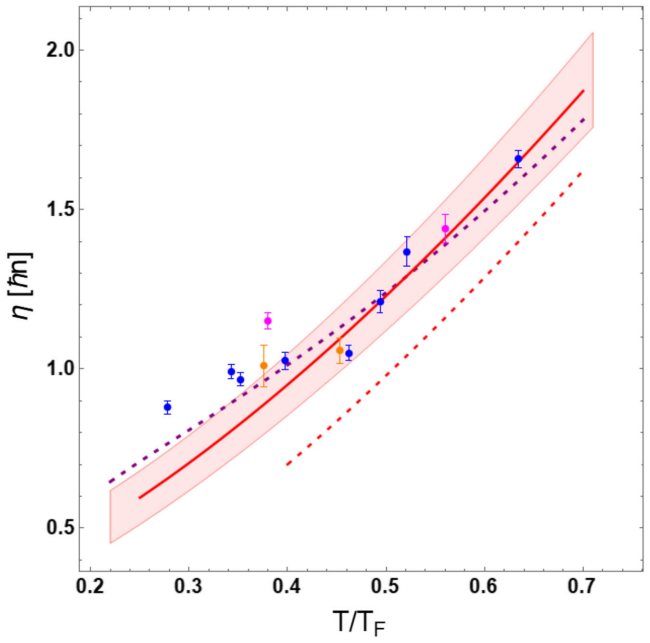

FIG. 3. Shear viscosity η in units of $\hbar n$ versus reduced temperature T/T_F. Blue dots: $\lambda \simeq 23$ μm. Orange dots: left (right) $\lambda = 18.2(18.9)$ μm. Pink dots: left (right) $\lambda = 32.3(41.7)$ μm. Red solid curve: fit to cloud expansion data, $\alpha_0\theta^{3/2} + \alpha_2$ (Bluhm *et al.*, [9], see text). Shaded region denotes the standard deviation of the fit. Upper purple-dashed curve: prediction of Enss *et al.*, [22]. Lower red-dashed curve: high temperature limit, $\alpha_0\theta^{3/2}$. Data error bars are statistical [23]. (color online).

The frequencies Γ, a, and b in Eq. (3) are related to the frequencies $\gamma_\eta \equiv 4\eta q^2/(3n_0 m)$, $\gamma_\kappa \equiv \kappa_T q^2/(n_0 c_{V_1})$, and $c_T q$ by [13]

$$\Gamma + 2a = \gamma_\kappa + \gamma_\eta \tag{4}$$

$$a^2 + b^2 + 2a\Gamma = c_S^2 q^2 + \gamma_\eta\gamma_\kappa \tag{5}$$

$$\Gamma(a^2 + b^2) = c_T^2 q^2 \gamma_\kappa. \tag{6}$$

Here, c_S and c_T are the adiabatic and isothermal sound speeds, which obey $c_S^2/c_T^2 = c_{P_1}/c_{V_1} = 1 + \epsilon_{\rm LP}(T/T_F)$.

Fitting Eq. (3) to the data yields the red curve in Fig. 2, with the three frequencies $c_T q, \gamma_\eta, \gamma_\kappa$, and the amplitude A as free parameters. We find that fitting the data with $A_0 = 0$ increases the χ^2 per degree of freedom from $\simeq$1 to $\simeq$20, demonstrating the importance of the thermal diffusion mode, which determines the thermal conductivity in our measurements.

The reduced temperature $T/T_F = \theta(c_T/v_F)$ in Eqs. (4)–(6) is self-consistently determined from c_T by the equation of state [13,14], with v_F given for the average central density n_0 [13]. The fits determine the frequency $c_T q$ within 2%, enabling *in situ* thermometry [19].

We note that in the long wavelength (LW) limit, where $c_S q \gg \gamma_\kappa, \gamma_\eta$, Eq. (5) requires $b/q \simeq c_S$, the first sound speed. Then Eq. (6) reduces to $\Gamma/q^2 \simeq \kappa_T/(n_0 c_{P_1}) = D_T$, the thermal diffusivity, and Eq. (4) yields $2a/q^2 \simeq \gamma_\eta/q^2 + \gamma_\kappa/q^2 - \Gamma/q^2 = D_1$, the usual first sound diffusivity [13,20]. In our experiments, where $\lambda \simeq 23$ μm, we find that b/q is smaller than c_S by 2.2%, 4.3%, and 5.7% for $T/T_F = 0.28$, 0.46, and 0.63, respectively, close to the LW limit.

Further, the LW limit requires $A_0/A = 1 - c_{V_1}/c_{P_1}$, which is $\simeq$0.3 for our T/T_F range and within 10% of the measured values. As a cross-check, we fit the data with Eq. (3), letting both A and A_0 be free parameters, and obtain consistent results for A_0/A.

We also estimate the change in the energy per particle W_1 that arises from the energy stored in the initial spatially periodic density profile. Assuming adiabatic compression, we find [13],

$$W_1 = \frac{mc_S^2}{2}\left\langle \left(\frac{\delta n}{n_0}\right)^2 \right\rangle. \tag{7}$$

For $\delta n/n_0 \simeq 0.2\cos(qz)$, we have $W_1 \simeq 0.01 mc_S^2$. As $mc_S^2 = 10/9E_1$, with E_1 the energy per particle [10,13], the change in E_1, and hence in $\theta = T/T_F$, is negligible.

Our measured shear viscosity, Fig. 3, can be compared to the high temperature diluteness expansion of Bluhm *et al.*, [9], $\eta_{\rm exp}(\theta) = (\alpha_0\theta^{3/2} + \alpha_2)\hbar n$, where $\alpha_0 = 2.77(21)$ and $\alpha_2 = 0.25(08)$ are measured by using a second order hydrodynamics model to fit aspect ratio data for freely expanding clouds [7]. Here, the first term is the high temperature limit, where $\theta^{3/2} n \propto T^{3/2}$ depends only on the temperature. The extracted α_0 is in excellent agreement with a variational calculation based on the two-body Boltzmann equation for a unitary gas [9,21]. The leading correction from α_2 depends only on the density. The red curve in Fig. 3 shows that $\eta_{\rm exp}(T/T_F)$ is in agreement with the measurements in the box potential for $T/T_F \geq 0.45$. For comparison, the red-dashed curve shows the high temperature limit, where $\alpha_2 = 0$. The top purple-dashed curve is the T-matrix theory prediction of Enss *et al.*, [22], in reasonable agreement with the data.

In all of the figures, we compare data for $\lambda \simeq 23$ μm to data points with $\lambda = 18.2$ μm, 18.9 μm, 32.3 μm (three-spatial periods), and 41.7 μm (two-spatial periods). These measurements show that there are no large systematic shifts with wavelength.

Our measured thermal conductivity, Fig. 4, can be compared with variational calculations for a unitary Fermi gas in the high temperature, two-body Boltzmann equation limit [24], where $\kappa_T(\theta) = 15/4\alpha_0\theta^{3/2}\hbar n\, k_B/m$, with k_B the Boltzmann constant. The red-dashed line in Fig. 4 shows that the high temperature prediction is in reasonable agreement with measurements in the box potential for $T/T_F \geq 0.45$,

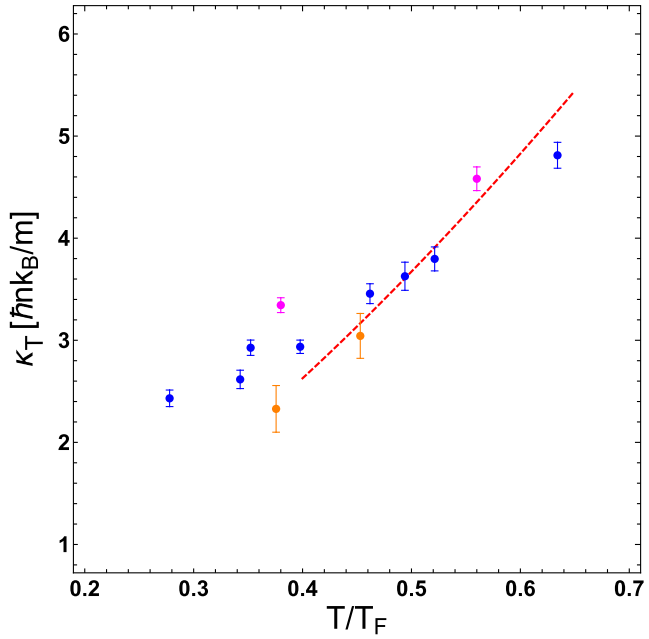

FIG. 4. Thermal conductivity κ_T in units of $\hbar n k_B/m$ versus reduced temperature T/T_F. Blue dots: $\lambda \simeq 23$ μm. Orange dots: left (right) $\lambda = 18.2(18.9)$ μm. Pink dots: left (right) $\lambda = 32.3(41.7)$ μm. Red-dashed curve: high temperature limit, $15/4\alpha_0\theta^{3/2}$. Error bars are statistical [23]. (color online).

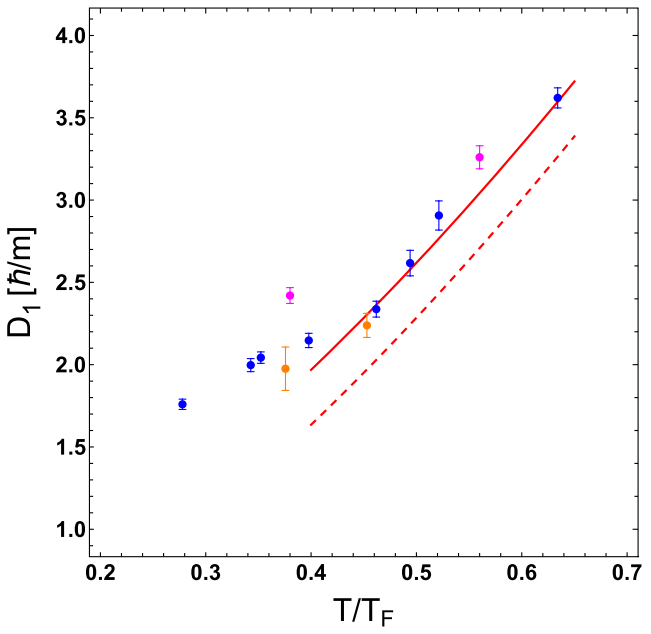

FIG. 5. Sound diffusivity $D_1 = 2a/q^2$, in units of $\hbar/m$ versus reduced temperature T/T_F. Blue dots: $\lambda \simeq 23$ μm. Orange dots: left (right) $\lambda = 18.2(18.9)$ μm. Pink dots: left (right) $\lambda = 32.3(41.7)$ μm. Red-dashed curve: long wavelength, high temperature limit, $D_1 = 7/3\,\alpha_0\,\theta^{3/2}$. Red solid curve: $D_1 = 4/3(\alpha_0\theta^{3/2} + \alpha_2) + \alpha_0\theta^{3/2}$. Error bars are statistical [23]. (color online).

without a temperature-independent correction, but the data are significantly smaller than predicted [25,26].

The sound diffusivity $D_1 = 2a/q^2$, in units of $\hbar/m$, Fig. 5, is determined by Eqs. (4)–(6) from the fit parameters $c_T q$, γ_η, and γ_κ. We obtain the same results within our error bars, by directly fitting Γ, a, and b in Eq. (3), constraining A_0/A using the LW limit, where $b \simeq c_S q$ determines T/T_F. The red-dashed curve shows the predicted LW D_1, using the high temperature limits for both the shear viscosity and the thermal conductivity, with $c_{P_1} = 5/2k_B$ and $c_{V_1} = 3/2k_B$. For the red solid curve, the high temperature shear viscosity term in D_1 is replaced with the measured viscosity for the expanding gas, $\eta_{\rm exp}(\theta)$, yielding a good fit for the higher temperature measurements, consistent with our measured η and κ_T. Our diffusivity data can be compared to that of Patel *et al.*, [10], which are shifted upward relative to that of Fig. 5, but exhibit nearly identical scaling with T/T_F, as discussed in the Supplemental Material [13].

In conclusion, we have independently determined the shear viscosity and thermal conductivity of a normal-fluid unitary Fermi gas in a box potential, directly from the two-mode oscillatory decay of a spatially periodic density perturbation. For the isothermal static initial conditions employed in the experiments, the thermally diffusive mode comprises ≃30% of the initial total amplitude of the dominant Fourier component, which is readily apparent in the free hydrodynamic relaxation. This method is complementary to frequency domain techniques, where transport properties of quantum fluids have been determined by measuring the hydrodynamic linear susceptibility [27–29]. For reduced temperatures $T/T_F > 0.45$, we find that the shear viscosity measured by free hydrodynamic relaxation in a box potential is consistent with that extracted from data on expanding clouds [8,9], which includes a significant density-dependent contribution. At lower temperatures, $T/T_F < 0.4$, the shear viscosity measured in the box is consistently larger than that of the expanding cloud. The thermal conductivity for $T/T_F > 0.45$ is close to the high temperature limit. In contrast to the shear viscosity, the pure density dependent contribution to the high temperature thermal conductivity appears to be quite small. These results emphasize the need for rigorous calculations of the leading density-dependent corrections to the two-body high temperature limits. Finally, we expect that in the superfluid regime, the exponentially decaying mode will evolve into an oscillating second sound mode, which we hope to study in future experiments.

We thank Thomas Schäfer for stimulating discussions and Parth Patel and Martin Zwierlein for providing their sound diffusivity data in table form. Primary support for this research is provided by the Physics Divisions of the National Science Foundation (PHY-2006234) and the Air Force Office of Scientific Research (FA9550-16-1-0378).

Note added in the proof.—Recently a related study has appeared [30].

*Corresponding author.
jethoma7@ncsu.edu

[1] A. Adams, L. D. Carr, T. Schäfer, P. Steinberg, and J. E. Thomas, Strongly correlated quantum fluids: Ultracold quantum gases, quantum chromodynamic plasmas and holographic duality, New J. Phys. **14**, 115009 (2012).
[2] G. C. Strinati, P. Pieri, G. Röpke, P. Schuck, and M. Urban, The BCS-BEC crossover: From ultra-cold Fermi gases to nuclear systems, Phys. Rep. **738**, 1 (2018).
[3] I. Bloch, J. Dalibard, and S. Nascimbène, Quantum simulations with ultracold quantum gases, Nat. Phys. **8**, 267 (2012).
[4] K. M. O'Hara, S. L. Hemmer, M. E. Gehm, S. R. Granade, and J. E. Thomas, Observation of a strongly interacting degenerate Fermi gas of atoms, Science **298**, 2179 (2002).
[5] T.-L. Ho, Universal Thermodynamics of Degenerate Quantum Gases in the Unitarity Limit, Phys. Rev. Lett. **92**, 090402 (2004).
[6] C. Cao, E. Elliott, J. Joseph, H. Wu, J. Petricka, T. Schäfer, and J. E. Thomas, Universal quantum viscosity in a unitary Fermi gas, Science **331**, 58 (2011).
[7] J. A. Joseph, E. Elliott, and J. E. Thomas, Shear Viscosity of a Unitary Fermi Gas Near the Superfluid Phase Transition, Phys. Rev. Lett. **115**, 020401 (2015).
[8] M. Bluhm and T. Schäfer, Model-Independent Determination of the Shear Viscosity of a Trapped Unitary Fermi Gas: Application to High-Temperature Data, Phys. Rev. Lett. **116**, 115301 (2016).
[9] M. Bluhm, J. Hou, and T. Schäfer, Determination of the Density and Temperature Dependence of the Shear Viscosity of a Unitary Fermi Gas based on Hydrodynamic Flow, Phys. Rev. Lett. **119**, 065302 (2017).
[10] P. B. Patel, Z. Yan, B. Mukherjee, R. J. Fletcher, J. Struck, and M. W. Zwierlein, Universal sound diffusion in a strongly interacting Fermi gas, Science **370**, 1222 (2020).
[11] A new method for directly measuring temperature waves has been reported recently, accessing second sound and thermal diffusion in a unitary Fermi gas. See Z. Yan, P. B. Patel, B. Mukherjee, R. Fletcher, and M. W. Zwierlein, DAMOP21/Session/U07.2.
[12] L. Baird, X. Wang, S. Roof, and J. E. Thomas, Measuring the Hydrodynamic Linear Response of a Unitary Fermi Gas, Phys. Rev. Lett. **123**, 160402 (2019).
[13] See the Supplemental Material at http://link.aps.org/supplemental/10.1103/PhysRevLett.128.090402 for discussions of the linearized hydrodynamic equations, the analytic solution, the sound diffusivity, the forces arising from the box potential, the determination of the density, and the systematic error arising from the density variation.
[14] M. J. Ku, A. T. Sommer, L. W. Cheuk, and M. W. Zwierlein, Revealing the superfluid lambda transition in the universal thermodynamics of a unitary Fermi gas, Science **335**, 563 (2012).
[15] For a unitary Fermi gas, the bulk viscosity ξ_B has been measured [16] and found to be negligible compared to the shear viscosity, consistent with predictions that $\xi_B = 0$ for scale invariant systems [17,18].
[16] E. Elliott, J. A. Joseph, and J. E. Thomas, Observation of Conformal Symmetry Breaking and Scale Invariance in Expanding Fermi Gases, Phys. Rev. Lett. **112**, 040405 (2014).
[17] D. T. Son, Vanishing Bulk Viscosities and Conformal Invariance of the Unitary Fermi Gas, Phys. Rev. Lett. **98**, 020604 (2007).
[18] Y.-H. Hou, L. P. Pitaevskii, and S. Stringari, Scaling solutions of the two-fluid hydrodynamic equations in a harmonically trapped gas at unitarity, Phys. Rev. A **87**, 033620 (2013).
[19] We give $\theta = T/T_F$ for the average central density n_0 [13].
[20] L. D. Landau and E. M. Lifshitz, *Fluid Dynamics, Course of Theoretical Physics Vol. VI* (Pergamon Press, Oxford, 1959).
[21] G. M. Bruun and H. Smith, Shear viscosity and damping for a Fermi gas in the unitary limit, Phys. Rev. A **75**, 043612 (2007).
[22] T. Enss, R. Haussmann, and W. Zwerger, Viscosity and scale invariance in the unitary Fermi gas, Ann. Phys. (Amsterdam) **326**, 770 (2011).
[23] The vertical error bars in Figs. 3 and 4 denote $\pm\sqrt{2\epsilon_{ii}}$, where ϵ_{ij} is the error matrix obtained from $\chi^2(\gamma_\eta, \gamma_\kappa)$ with A and c_T fixed. For the diffusivity in Fig. 5, ϵ_{aa} is found from $\chi^2(a, b)$, minimizing with respect to A and Γ, holding c_T fixed in Eq. (3). We estimate a systematic downward shift of $\leq 5\%$, arising from the density variation [13].
[24] M. Braby, J. Chao, and T. Schäfer, Thermal conductivity and sound attenuation in dilute atomic Fermi gases, Phys. Rev. A **82**, 033619 (2010).
[25] B. Frank, W. Zwerger, and T. Enss, Quantum critical thermal transport in the unitary Fermi gas, Phys. Rev. Research **2**, 023301 (2020).
[26] H. Zhou and Y. Ma, Thermal conductivity of an ultracold Fermi gas in the BCS-BEC crossover, Sci. Rep. **11**, 1228 (2021).
[27] P. C. Hohenberg and P. C. Martin, Microscopic theory of superfluid helium, Ann. Phys. (N.Y.) **34**, 291 (1965).
[28] H. Hu, P. Zou, and X.-J. Liu, Low-momentum dynamic structure factor of a strongly interacting Fermi gas at finite temperature: A two-fluid hydrodynamic description, Phys. Rev. A **97**, 023615 (2018).
[29] P. Zhang and Z. Yu, Energy-absorption spectroscopy of unitary Fermi gases in a uniform potential, Phys. Rev. A **97**, 041601(R) (2018).
[30] X. Li, X. Luo, S. Wang, K. Xie, X.-P. Liu, H. Hu, Y.-A. Chen, X.-C. Yao, and J.-W. Pan, Second sound attenuation near quantum criticality, Science **375**, 528 (2022).